Electrical characterization of co-precipitated $LaBaCo_2O_{5+\delta}$ and $YBaCo_2O_{5+\delta}$ oxides

Renato Pelosato [a,*], Alessandro Donazzi [b,**], Giovanni Dotelli [a], Cinzia Cristiani [a], Isabella Natali Sora [c], Mario Mariani [b]

[a] *Politecnico di Milano, Dipartimento di Chimica Materiali e Ingegneria Chimica "G. Natta", Piazza Leonardo da Vinci 32, 20133 Milano, Italy*
[b] *Politecnico di Milano, Dipartimento di Energia, Via Lambruschini 4, 20156 Milano, Italy*
[c] *INSTM R.U. and Università di Bergamo, Dipartimento di Ingegneria, Viale Marconi 5, 24044 Dalmine, BG, Italy*

Received 10 June 2014; received in revised form 1 July 2014; accepted 4 July 2014
Available online 5 August 2014

1. Introduction

A-site ordered perovskite oxides with general formula $REBaCo_2O_{5+\delta}$ (*RE* = Rare Earths) have been traditionally investigated for their low-temperature electrical and magnetic properties,[1,2] and more recently they raised considerable interest in the Solid Oxide Fuel Cell (SOFC) community as promising low temperature cathodes; several studies were therefore devoted to investigate their high temperature properties, especially the crystal structure, the electrical conductivity and the electrochemical performance.[3–10] The most important characteristic of these compounds is the ordering of the A-site cations in alternating layers, *RE*-O, Co-O, Ba-O, Co-O along the *c*-axis of the perovskite lattice. The properties that make these materials promising as low temperature cathodes are the high electronic conductivity at intermediate temperatures, the high oxygen vacancy concentration, the good ion transport activity and the very high oxygen surface exchange coefficients, if compared to A-site disordered perovskites.[7,11,12] This class of compounds can accept a wide range of oxygen stoichiometries ($0 \leq \delta \leq 1$), driven by the mean Co oxidation state; the oxygen content in the final material depends on the size of the *RE* cation, but it can also be governed by the annealing conditions. As the size of the *RE* cation decreases, the oxygen content at room temperature decreases from nearly 6 for La (either in ordered or disordered structure), ~5.7 for Pr and Nd, ~5.5 for Y, ~5.4 for Sm, Eu, Gd and Tb, down to ~5.3 for Dy and Ho. These values typically vary depending on the treatment atmosphere and the preparation procedure. Moreover, the oxygen content decreases upon increasing the temperature. Interestingly, a linear relationship has been reported between the oxygen content and A-site ionic radii difference $[r_{(RE)} - r_{(Ba^{2+})}]$.[12]

* Corresponding author. Tel.: +39 02 2399 3232; fax: +39 02 7063 8173.
** Corresponding author. Tel.: +39 02 2399 8651; fax: +39 02 2399 3318.
E-mail addresses: renato.pelosato@chem.polimi.it (R. Pelosato), alessandro.donazzi@polimi.it (A. Donazzi).

Also, the relative ionic radii of the two A-site cations drives structural transitions in these compounds.[5] When the size difference between *RE* and Ba is small, the disordered structure is preferentially obtained; nonetheless, the ordered structure can be achieved by carefully tailoring the annealing temperatures and the preparation atmospheres, as in the case of *RE* = La.[13] Overall, the defect chemistry of both ordered and disordered perovskite structures appears to have a great influence on the electrochemical properties of these materials.

Our group has recently applied a simple carbonate co-precipitation technique to synthesize mixed oxides with perovskite structure for application in Solid Oxide Fuel Cells. Reasonably good materials were obtained, both for the electrolyte[14,15] and the electrodes,[16] with fair conduction properties and stability, despite some deviations from the ideal stoichiometries. Several reasons make the coprecipitation a valuable preparation technique. The coprecipitation synthesis allows to achieve a very intimate mixing of the perovskite precursors, in the present case in form of carbonates and hydroxides. A homogenous precipitate is obtained, with fine grain size distribution. The achievement of small grain sizes depends on the operating conditions of the synthesis, namely temperature, pH, nature and concentration of the precursors, parameters that can be tailored and controlled during the preparation. The perovskite phase is obtained via one-step calcination, at the same temperature generally required by other techniques: the final material retains the original homogeneity and a fine grain size, compatibly with some expected sinterization. Compared to the solid state preparation route (the most widespread synthesis method for SOFC materials), considerable amount of energy is saved by mixing liquid solutions instead of solid powders, thus avoiding expensive and time-consuming milling steps. In the present work, the carbonate co-precipitation method is proposed for the preparation of $RE BaCo_2O_{5+\delta}$ with *RE* = La and Y (hereafter referred to as LBC and YBC respectively). Disordered structure of $LaBaCo_2O_6$ and ordered $YBaCo_2O_{5+\delta}$ perovskites were adopted as model compounds to assess the suitability of the preparation route. The evaluation of the co-precipitation method on $RE BaCo_2O_{5+\delta}$ layered perovskites faces the challenge of finding the proper conditions for the quantitative precipitation of all the desired cations, which in turn influence the obtainment of the target stoichiometry. In particular, two conflicting challenges must be overcome: the hydroxides of alkaline earth metals (Ba in the present case) show a slight, non-negligible, solubility in water, therefore some losses might be expected during the preparation. The second challenge concerns the stability of $Co–NH_3$ complexes in basic environments, which prevents the precipitation of Co as carbonate or hydroxide. To deal with these drawbacks, in this work, equilibria calculations were performed with the Medusa software[17] and the experimental conditions of the preparation were maintained as close as possible to the optimal thermodynamic indications. For each material prepared, the powders were characterized via X-ray diffraction, SEM–EDS, TG–DTA and TPO analyses. The electrochemical properties were also evaluated by measuring the total electrical conductivity, via 4-probe method on sintered bars, and the polarization behavior, via electrochemical impedance spectroscopy (EIS), on symmetric cell configuration. In the case of LBC, good results were achieved and a quantitative electro-kinetic study on the impedance spectra was proposed. In the case of YBC, even though it has been recently revealed that the structure is unstable at high temperature in air,[18] the electrochemical performances of the as-synthesized material allowed to draw positive conclusions about the goodness of the preparation route (also in view of structure-stabilization via substitution of Ba with Sr[18]).

2. Materials and methods

2.1. Synthetic procedure

$La(NO_3)_3{\cdot}6H_2O$ (99.99%, Sigma–Aldrich), $Y(NO_3)_3{\cdot}4H_2O$ (99.99%, Sigma–Aldrich), $Ba(NO_3)_2$ (99%, Sigma–Aldrich), $Co(NO_3)_2{\cdot}6H_2O$ (99%, Sigma–Aldrich) salts were used as precursors in the co-precipitation synthesis; the precipitating agent was $(NH_4)_2CO_3$ and the solvent was distilled water. The synthetic procedure is reported in details elsewhere.[16] Briefly, the procedure simply involves the addition of a solution of the nitrates of the constituents to a solution of the precipitating agent with the proper concentrations, followed by a 3 h aging period and a filtration step to separate the precipitates from the solution. The evaluation of the optimal precipitation conditions was performed by calculating the theoretical precipitation equilibria, using the Hydra thermodynamic database and the Medusa software.[17] In the calculations, different simulations were performed by changing the concentration and amount of the precipitating agent, while keeping constant the concentrations of the metal salts. The solution volume was also kept constant and equal to the sum of the volumes of the metal salt solution and of the precipitating agent solution. Plots of the calculated fraction of species at equilibrium vs. pH were used to estimate the optimal precipitating agent concentration and pH range.

After the filtration process, the powders were desiccated at 110 °C and then crushed in a mortar and fired at temperatures up to 1000 °C in air, with heating and cooling rates of 2 °C/min and dwell time of 10 h. After the filtration process, the solutions were collected and analyzed via Inductively Coupled Plasma-Mass Spectrometry (ICP-MS, Thermo X series II instrument) to search for any metal ion left.

2.2. Powders characterization

The powders of the two materials were characterized by X-ray diffraction (XRD) with a Bruker D8 instrument, using graphite monochromated Cu K_α radiation; the diffraction patterns were collected in the range 10–80° 2θ with a step of 0.02° 2θ and a counting time of 12 s per step. The XRD spectra of the samples fired at 1000 °C were refined with the Rietveld method[19] using the GSAS software[20] for the determination of the structural parameters. XRD analyses were carried out also on mechanical mixtures (50/50 wt%) of YBC and LSGM, as well as of LBC and LSGM. The mixtures were fired at different temperatures to evaluate the occurrence of any chemical interaction between the electrolyte and the cathode, 1100 °C in the case of YBC and 900 °C in the case of LBC. These two temperatures are those

that guarantee adhesion of the cathode layers to the LSGM electrolyte during the preparation of the symmetric cell (details are given in Section 2.3).

The precursor powders (after drying at 110 °C) and the final powders (after calcination at 1000 °C) were analyzed via scanning electron microscopy (SEM) carried out with a Carl Zeiss EVO50VP instrument equipped with an energy dispersive spectrometer (EDS) for elemental analysis.

Thermogravimetric analyses (TG–DTA) were performed on 30 mg of the calcined samples by a simultaneous TG-DTA Seiko 6300 instrument. In a TG–DTA experiment, the powders were heated in air from room temperature to 1050 °C at 5 °C/min, and then cooled in air to room temperature, again at 5 °C/min.

Temperature Programmed Oxidation (TPO) tests were performed on the cathode materials in order to investigate the oxidation behavior. The TPO tests were carried out with 150 mg powder samples, in a Micromeritics AutoChem II instrument equipped with a TCD detector and with a trap for the adsorption of water and CO_2. A TPO test consisted of three repeated heating and cooling cycles between 50 and 950 °C, under diluted O_2 flow (20 Ncc/min, 2% O_2 in He). During each cycle, the sample was heated from 50 °C to 950 °C at 2 °C/min, held at 950 °C for 1 h and cooled to 50 °C at 2 °C/min. Prior to the admission of the O_2 flow, the sample was first evacuated in He (20 Ncc/min) at 120 °C for 1 h and then cooled down to 50 °C. The oxidation reaction of copper III oxide ($Cu_2O_3 + 1/2O_2 \rightarrow 2\,CuO$) performed under identical conditions of the TPO (150 mg Cu_2O_3, 20 Ncc/min, 2% O_2 in He, 2 °C/min ramp rate) was applied as a calibration standard for the quantification of the signals.

2.3. Electrical characterization

The electrical properties of the two materials were characterized in terms of total electrical conductivity and polarization behavior. A potentiostat/galvanostat (Amel 7050) equipped with a frequency response analyzer (510 V10, Materials and Mates) was used for the measurements.

The total electrical conductivity was measured with a DC four-probe method on sintered bars. The bars (24 mm length × 4.5 mm width × 2 mm thickness) were obtained by die-pressing the powders (10,000 kg/cm^2) and subsequent calcination at 1000 °C for 5 h in air. The density of each bar was determined by weighting with a buoyancy balance, using water as the wetting media, to verify that sufficiently high sintering was achieved. The electrodes were painted with Ag conductive paste (RS) and were fixed to the current leads by calcination in air at 800 °C. The conductivity was determined in flowing air (100 Ncc/min) between 25 and 800 °C, by applying a constant current and measuring the output voltage. The current was stepwise increased from 1 mA to 1 A, and sufficient time (10 min) was given to the sample to stabilize the voltage response.

Electrochemical impedance spectroscopy (EIS) tests were performed to characterize the polarization behavior. The tests were performed using a symmetric cell configuration with LSGM as the electrolyte material. For each symmetric cell, a pellet (11 mm diameter) was fabricated from commercial LSGM powders ($La_{0.8}Sr_{0.2}Ga_{0.8}Mg_{0.2}O_{3-\delta}$, Fuel Cell Materials) via die-pressing (5000 kg/cm^2) and subsequent calcination at 1450 °C for 5 h in air. The sinterization of each pellet was verified by comparing the density value measured with the buoyancy balance (6.46 g/cm^3) and 98% of the theoretical density was achieved. A slurry of the cathode material (50 wt% solid content) was prepared from the powders, by adding α-terpineol, isopropyl alcohol and ethyl cellulose (76:20:4 relative weights) and stirring the mixture for 2 h. The slurry was applied on each side of the electrolyte substrate as symmetrically as possible. After the application, each layer was dried at 150 °C for 1 h in air. In order to achieve complete adhesion of the layers with the LSGM electrolyte, each cell was calcined at the lowest temperature level that guaranteed adhesion. SEM microscopy was used to verify the thickness of the layers. Knowing the thickness, the layers porosity was estimated from the weight and the density values. In the case of the LBC layers, adhesion was achieved after calcination at 900 °C for 4 h in air. The resulting layers were ∼15 μm thick, which corresponded to ∼65% porosity. In the case of the YBC layers, the adhesion was achieved only after calcination at 1100 °C for 4 h in air. The resulting layers were ∼30 μm thick, which corresponded to ∼68% porosity.

The EIS tests were performed at open circuit voltage in the frequency range 0.1 Hz–10 kHz, with a signal amplitude of 40 mV. Ag meshes and ink were applied on each side of the cell to form the current collecting electrodes. EIS tests were performed in flowing air (100 Ncc/min on each side of the cell) between 650 and 800 °C. Additionally, at each temperature level, tests at varying O_2 partial pressure (5, 10, 21 and 100%, v/v) were performed, both using N_2 and He as the O_2 diluent. The tests in flowing air were repeated up until the reaching of 500 h time on stream, in order to investigate the aging process of the materials.

3. Results and discussion

3.1. Precipitation conditions

Precipitation equilibria calculation relative to the actual precipitation experiments are reported in Fig. 1 (for the sake of clarity, only the solid species and the relevant complexes are included in the graphs). On the one hand, at low pH the formation of soluble $Ba(NO_3)_2$ hinders a successful precipitation of Ba component, therefore the low pH region must be avoided; on the other hand, at high pH the formation of Co–NH_3 complexes prevents the precipitation of Co. For both YBC (panel A) and LBC (panel B), the pH windows suitable for the quantitative precipitation of all cations is quite narrow, in the range 7.4–8.5. It is worth noting that the pH of the solution is regulated exclusively by addition of ammonium carbonate, with no use of strong basis (e.g. NaOH or KOH), which would force to several washing steps to remove residual ions from the precipitated material. Hence, there is a strict interplay between the target pH and the need of avoiding the complexation of Co. As a result, the experimental conditions must be a balance between these two conflicting goals; in both cases, the pH reached in the experiment was 7.4. This pH was kept constant starting right after the precipitation and during 3 h of aging. After the filtration of the

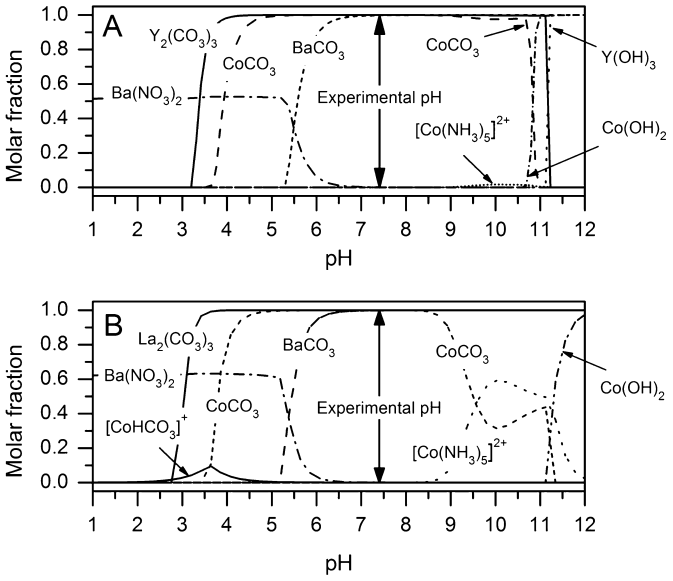

Fig. 1. Precipitation equilibria simulations for (a) YBC and (b) LBC solutions. Arrows indicate the experimental precipitation pH.

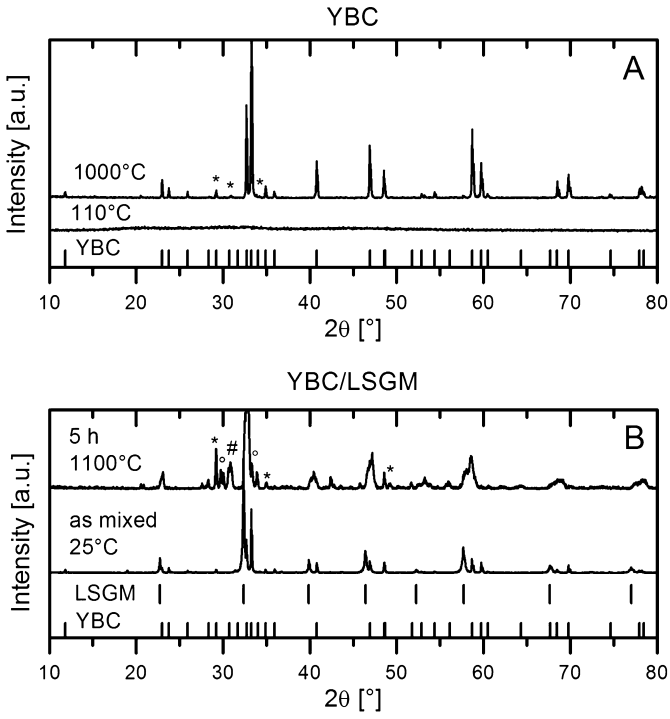

Fig. 2. XRD patterns of YBC at different temperatures. (Panel a) Pure YBC; unidentified phase (*). (Panel b) YBC/LSGM mixture (50/50 wt%); $LaBaGa_3O_7$ (o); Y_2O_3 (*); unidentified phase (#). Vertical bars are PDF #47-0735 for YBC and PDF #89-4448 for LSGM.

precipitates, the solutions were analyzed: the precipitation was quantitative for Y (in YBC) and La (in LBC). Some amounts of Ba and Co ions instead were revealed in the solutions: in YBC, about 9% of the starting Ba remained in the solution as well as 1% of the original Co. The result well agrees with the prediction of Fig. 1A, as the experimental precipitation pH touches the $Ba(NO_3)_2$ curve. In LBC instead, 8% of the original Ba and 4% of the starting Co were found in the solution. From Fig. 1B, the experimental pH in this experiment is halfway between the soluble $Ba(NO_3)_2$ compound and $[Co(NO_3)_5]^{2+}$ complex. These losses led to an alteration of the real stoichiometries with respect to the nominal ones: accordingly, the estimated stoichiometries are $YBa_{0.91}Co_{1.98}O_{5+\delta}$ for YBC and $LaBa_{0.92}Co_{1.92}O_{5+\delta}$ for LBC.

3.1.1. *Characterization of the YBC powders*

The XRD patterns of the dried YBC precursor and of the calcined powder are reported in Fig. 2a. The precipitated powder after desiccation at 110 °C is completely amorphous. After calcination at 1000 °C for 10 h the XRD pattern matched that of $YBaCo_2O_{5+\delta}$ (PDF #047-0735) with a tetragonal crystal structure. Just three weak reflections at $2\theta \sim 29.2°$, ~30.9° and ~34.0° remained unidentified. The pattern was refined with the Rietveld method using the tetragonal primitive cell (space group *P4/mmm*) described by Vogt et al.[21] for $YBaCo_2O_5$ above 330 K. The weak reflections at $2\theta \sim 29.2°$, ~30.9° and ~34.0° that could not be indexed were excluded from the refinements. Refined cell parameters are $a = 3.8769(1)$ Å, $c = 7.5017(4)$ Å, and the cell volume is 112.75 Å^3, slightly smaller than those in Ref.,[21] but in agreement with those reported by Akahoshi and Ueda[22] for samples with oxygen content between 5.15 and 5.19 at room temperature. With respect to the results of Vogt et al. referenced above, it is worth noting that in our sample the partial occupancy for Ba was found to be 0.96(1), in agreement with the chemical analysis (Section 3.1), and it may account for the differences in cell volume.

The XRD pattern of the YBC/LSGM mechanical mixture (Fig. 2B) reveal that strong interactions occurred after calcination at 1100 °C for 5 h: the comparison between the pattern of the mechanical mixture (25 °C) and the calcined one shows that Y_2O_3 (*) and $LaBaGa_3O_7$ (o) peaks appear, accompanied by other unidentified and intermediate peaks (#).

The dried precursor and the calcined powders were analyzed with a scanning electron microscope: SEM micrographs are shown in Fig. 3. The dried precursor (Fig. 3A) is mainly made of small particles with size of a few hundreds of nanometers, and show little agglomeration; as suggested by the XRD pattern, no crystalline habits could be detected. After calcination at 1000 °C (Fig. 3B), the average grain size is in the range of few micrometers, and necking between the particles developed; overall, the powder show a continuous structure with diffuse open porosity. This result suggests that a high surface area is retained after the high temperature firing.

3.1.2. *Characterization of the LBC powders*

The XRD pattern of LBC precursor and calcined powder are reported in Fig. 4A. The dried precursor (110 °C) is amorphous. After calcination at 1000 °C a perovskite phase developed, apparently matching the cubic pattern of $La_{0.5}Ba_{0.5}CoO_3$ (PDF # 032-0480), with a small amount of Co_3O_4 (*) and a possible doubling of some peaks. For the perovskite phase $La_{1-x}Ba_xCoO_3$ two crystallographic regions are known: rhombohedral symmetry for $0 \leq x < 0.35$ (space group *R-3c*), and

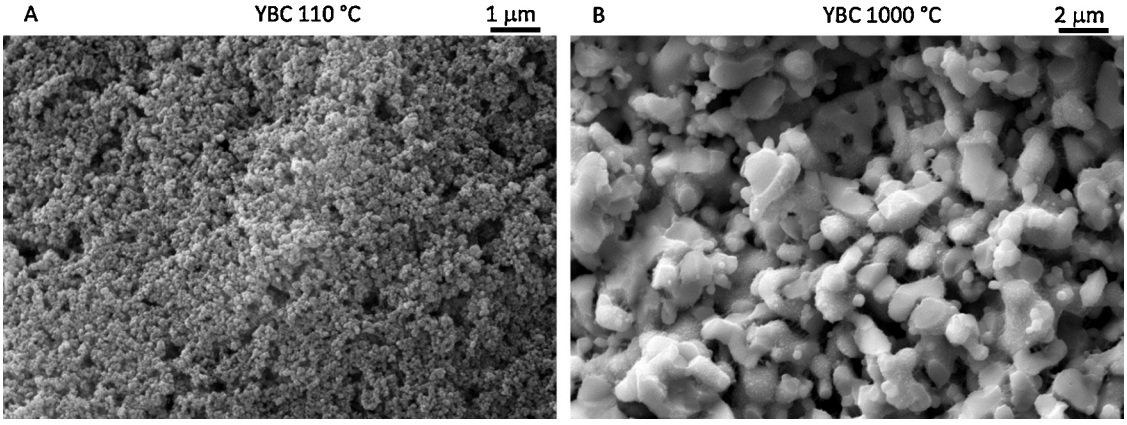

Fig. 3. SEM micrographs of (a) YBC precursor dried at 110 °C; (b) YBC powder calcined at 1000 °C.

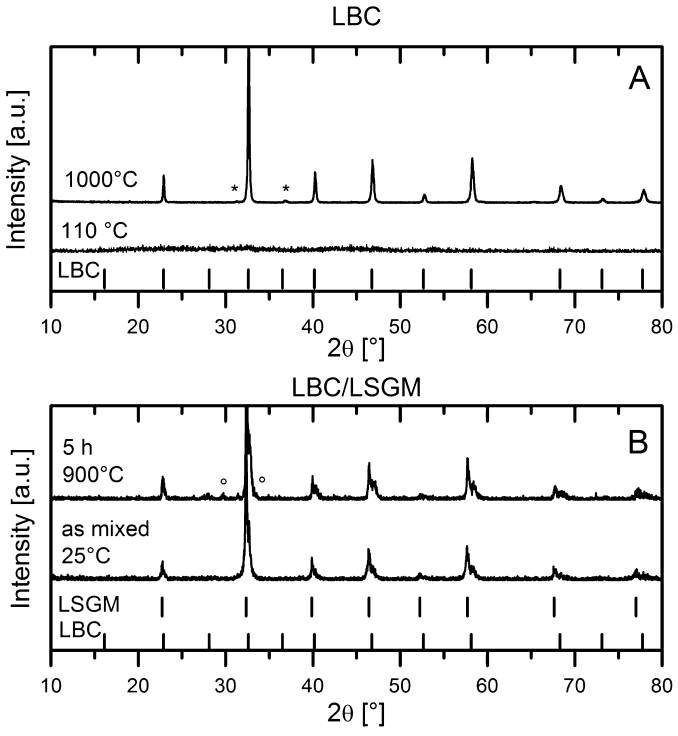

Fig. 4. XRD patterns of LBC at different temperatures. (Panel a) Pure LBC; Co_3O_4 (*). (Panel b) LBC/LSGM 50/50 wt% mixture; $LaBaGa_3O_7$ (o). Vertical bars are PDF #32-0480 for LBC and PDF #89-4448 for LSGM.

cubic symmetry for $0.4 \leq x \leq 1.0$ (space group *Pm-3m*).[23] Since the chemical analysis suggests a barium poor composition, attempts were made to refine the structure with both symmetries, resulting in better refinement indices for the cubic symmetry model ($\chi^2 = 2.78$, $R_B = 12.5\%$). The amount of Co_3O_4 (space group *Fd3m*) was about 10 wt%. Moreover, a large improvement in the refinement indexes ($\chi^2 = 1.71$, $R_B = 9.5\%$) was obtained by using a three-phase model, two slightly different structures of $(La_{1-x}Ba_x)CoO_3$, one cubic *Pm-3m* (about 50 wt%) and one tetragonal *P4/mmm* (about 40 wt%) which was reported by Fauth et al. for $La_{0.5}Ba_{0.5}CoO_3$ below 180 K,[24] and Co_3O_4 (about 10 wt%). The final refinement was carried out with the La to Ba ratio equal to 0.6:0.4 for both phases (from chemical analysis data), since La and Ba have similar electronic configuration, and it is not possible to perform reliable refinements of their site occupancy with laboratory X-ray diffractometer. The refined cell parameters are $a = 3.85608(8)$ Å for the cubic structure, and $a = 3.86176(8)$ Å, $c = 3.87652(18)$ Å for the tetragonal structure. The cubic unit cell is smaller than that reported for $La_{0.5}Ba_{0.5}CoO_3$ compound ($a = 3.8843$ Å),[24] due to the Ba understoichiometry, given the smaller ionic radius of La^{3+} ion (1.36 Å) with respect to Ba^{2+} ion (1.61 Å), while the tetragonal unit cell well agrees with previous work ($a = 3.8683$ Å, $c = 3.8748$ Å).

Slight changes are revealed in the XRD of LBC/LSGM mixture fired at 900 °C 5 h (Fig. 4B) in comparison with the XRD of the as-mixed one. The interaction required to bond the two layers yielded the formation of a small amount of $BaSrGa_3O_7$ (°). This result is somewhat in disagreement with the report of Kim and Manthiram,[5] where no reaction was claimed between LSGM and LBC at 1100 °C for 0.5 h; given that no information was provided by the authors about the microstructure of the materials, we can expect this different reactivity could be ascribed to a difference in particle size of the reacting powders, remembering that the LBC in Ref.[5] was prepared via solid state reactive firing, that usually causes growth of large grain sizes that could delay reaction with the electrolyte powder.

LBC powder microstructure is reported in the SEM micrographs of Fig. 5: the dried precursor powder is fine grained with some agglomerated particles; no crystalline habits could be detected, supporting the XRD data. The calcined powder (1000 °C) kept an extremely small average grain size that can be estimated in few hundreds of nanometers, with some necking between the particles. Apparently, a very high surface area could be retained after the calcination step, which is a desirable feature for the preparation of electrode materials.

3.1.3. YBC oxidation behavior

The results of the TG–DTA experiment performed under air flow are reported in Fig. 6A. In the plot, until about 200 °C, the desorption of moisture and adsorbed CO_2 is mainly responsible for the weight change, whereas, above this temperature, it can be assumed that the weight losses are due to changes in O_2 content of the structure, coherently with Refs.[5,6] Upon heating, a weight loss is observed up to 950 °C, which amounts to

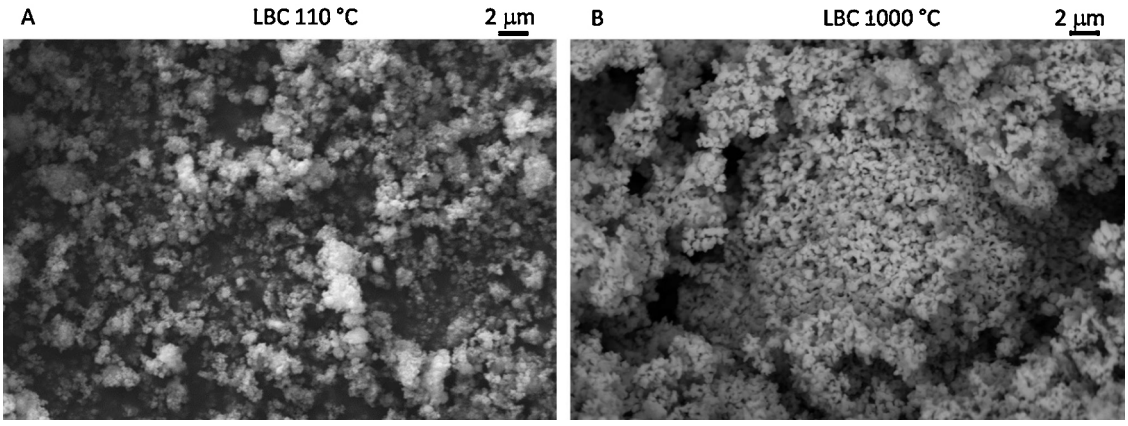

Fig. 5. SEM micrographs of (a) LBC precursor dried at 110 °C; (b) LBC powder calcined at 1000 °C.

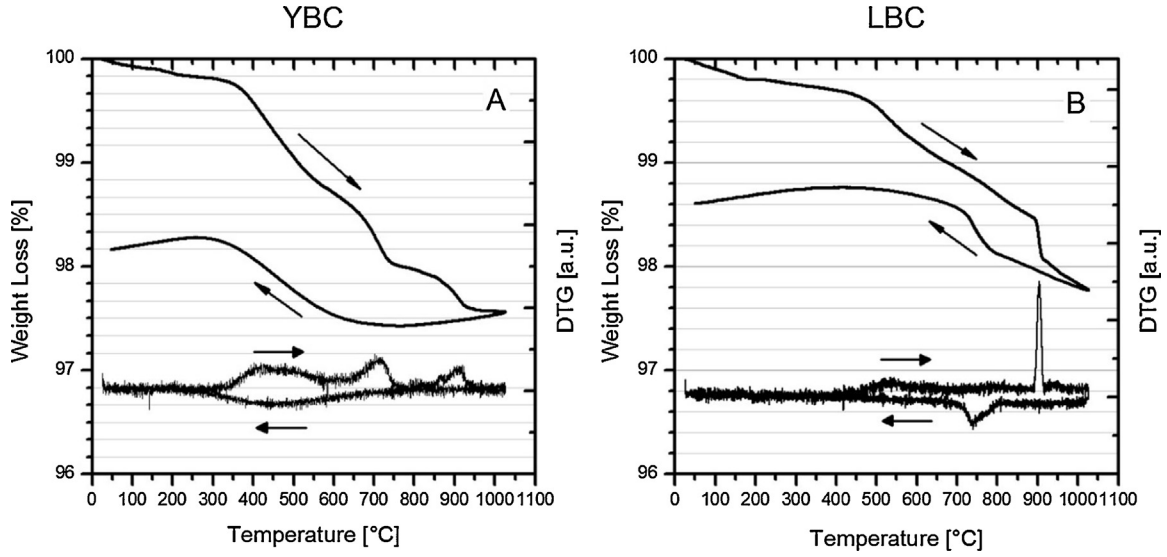

Fig. 6. TG–DTG curves of (a) YBC and (b) LBC samples. Operating conditions: air flow, $T_{ramp} = 5\,^{\circ}C/min$, $T_{MAX} = 1050\,^{\circ}C$. (Panel A) YBC. (Panel B) LBC.

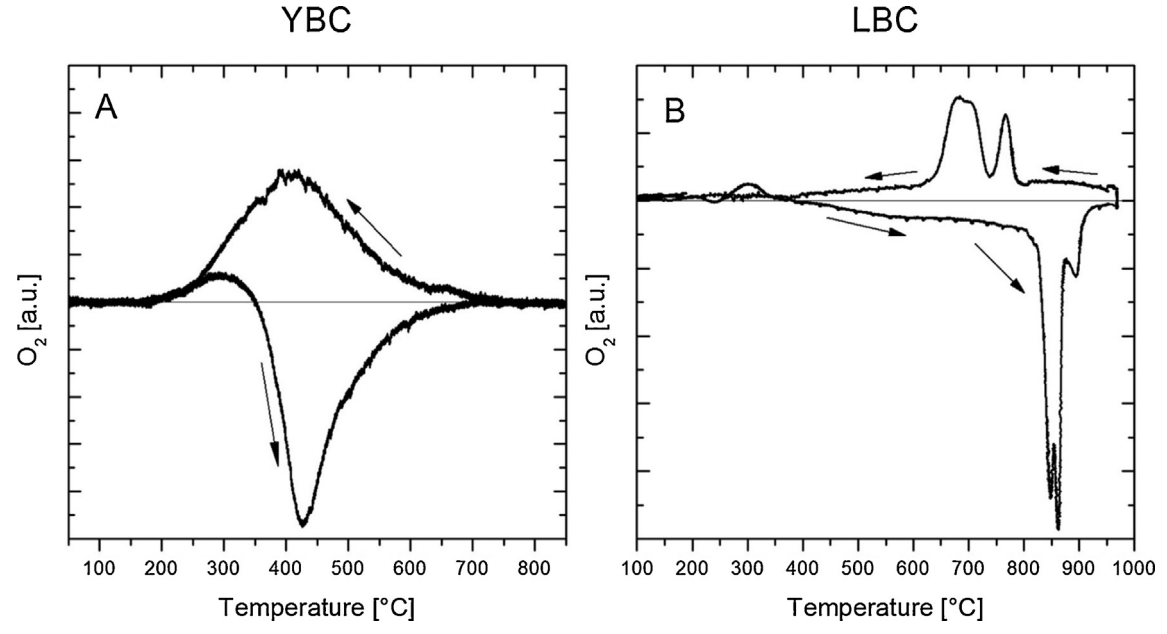

Fig. 7. O_2 evolution as a function of temperature during the heating and the cooling ramp of a Temperature Programmed Oxidation experiment. Operating conditions: $O_2 = 2\%$, He = 98%, flow rate = 20 Ncc/min, $T_{MIN} = 50\,^{\circ}C$, $T_{ramp} = 2\,^{\circ}C/min$, $T_{MAX} = 950\,^{\circ}C$. (Panel A) YBC. (Panel B) LBC.

Table 1
Fractional weight gain and weight loss of the YBC and the LBC samples estimated on the basis of the O_2 released and consumed during the TPO cycle. Operating conditions as in Fig. 7.

Cycle	Ramp	Weight (%)
YBC	Heating	−0.64
	Cooling	+0.79
LBC	Heating	−0.89
	Cooling	+0.90

2.2 wt% of the initial weight. This loss is accompanied by three O_2 desorption peaks in the DTG profile, two of which are located between 400 and 700 °C, while a third, late, one is located around 900 °C. During the cooling phase, the sample regains approximately 0.4 wt% of its initial weight, giving rise to one single O_2 adsorption peak in the DTG profile. The redox behavior of the Co^{4+}/Co^{3+} couple is generally reported as responsible for the variation of the oxygen content: namely, Co reduces upon heating, as the equilibrium oxygen content decreases at increasing temperature, and re-oxidizes upon cooling. The TG–DTA results are in agreement with those reported by Kim et al.[5] for YBC samples, i.e. a weight loss of ∼1 wt% up to 850 °C. A behavior close to that of the thermogravimetric analysis is observed in the TPO experiment carried out with 2% O_2 in He flow (Fig. 7A). Compared to air, the smaller concentration of O_2 allows to better appreciate the adsorption/desorption pattern and to point out additional features. During the heating ramp, the TPO curve shows that O_2 is first adsorbed between 250 and 350 °C (positive peak) and then desorbed between 350 and 700 °C (negative peak). At temperatures higher than 700 °C, no further activity is apparent. The presence of the initial O_2 gain indicates that incomplete oxidation occurred during the cooling of the sample in the furnace after the synthesis firing, being likely associated with the oxidation of some fraction of Co^{3+}. Upon cooling the sample from 950 to 50 °C, a single broad peak of O_2 adsorption is observed, which slowly activates around 700 °C and completes around 250 °C. This behavior was steadily reproduced also during successive cycles (not reported). The amount of O_2 adsorbed and released is shown in Table 1 in terms of weight fractions, calculated as the ratio between the weight of O_2 gained or lost and the initial weight of the YBC sample. A single negative value is reported for the heating ramp, which is the sum of the gain observed at low temperature and the depletion that occurs at higher temperature. In this case, the exchanged O_2 amount maintains constant and no net loss is detected between the heating and the cooling ramp. Within the precision of both the techniques, the TPO results and the TG–DTA results are in reasonable agreement. Indeed, oxidation and re-oxidation processes are driven by kinetics, which means that they are determined by O_2 surface-exchange and bulk-diffusion rates, as well as by the size of the sample particles and the heating rate. In the present tests, the lower O_2 partial pressure may have shifted the peak temperature for the activation of the late desorption process (>900 °C) observed in the TG–DTA experiment; as well, the lower O_2 partial pressure may have changed the overall amount of O_2 being cycled.

3.1.4. LBC oxidation behavior

The oxidation behavior of the LBC sample was first characterized by TG–DTA analysis in air (Fig. 6B). Again, it can be assumed that low temperature desorption is due to humidity and CO_2 ($T < 200$ °C), whereas at higher temperature only O_2 is involved. The TG profile shows a steady decrease, up to 900 °C and ∼1.4 wt% of the initial weight. At about 900 °C, a further steep decrease is observed, which is accompanied by a sharp peak in the DTG profile. At 1000 °C, the final loss amounts to ∼2.2% of the initial weight. The cooling ramp allows the sample to regain only about half of the weight lost during the heating phase. Interestingly, a peak of O_2 re-adsorption appears, although shifted to lower temperature (750 °C) compared to the loss peak. These results are in agreement with those of Karan et al.,[25] who report an irreversible weight loss of 1.8% upon heating up to 800 °C, as well as with those of Kim et al.[5] and Pang et al.[26] (∼1.3% weight loss at 850 °C). The results of the TPO cycles (Fig. 7B) confirm those of the TG–DTA experiment, and also show additional fine features: during the heating ramp, a small positive O_2 adsorption peak is revealed at ∼300 °C, again suggesting the occurrence of incomplete oxidation during the synthesis firing. Upon increasing the temperature, a steady weight loss is apparent up to ∼850 °C, after which the occurrence of the strong O_2 desorption process is confirmed. The profile suggests that the desorption reaction involves at least three steps, each associated to a peak, at 852 °C, 862 °C and 895 °C. Upon cooling the sample, progressive weight gain is observed, followed by two O_2 adsorption peaks, a first one at about 750 °C and a second, larger one, at 650 °C. Hence, also in this case, the temperature threshold for O_2 re-adsorption is shifted to lower temperatures than the O_2 desorption. At the end of each cycle (reproduced for three times), the sample restores its initial O_2 content: the quantification of the TPO signals (Table 1) shows that ∼1% weight is exchanged between the heating and cooling phases.

As discussed in the case of YBC, the TPO and the TG–DTA results are in reasonable agreement when considering the fact that the redox behavior is driven by kinetics, so that the different O_2 partial pressure may have modified the peak temperatures and the reaction rates. The two analyses confirm the slow O_2 desorption upon ramping the temperature up to 800 °C, in line with what generally documented in the literature. Additionally, the two analyses confirm the occurrence of the strong O_2 desorption process at 900 °C, mirrored by a late O_2 re-adsorption. The presence of a desorption peak at about 900 °C was reported by Zhang et al.[6] during O_2-TPD experiments under N_2 flow: a series of layered Co-based perovskite oxides were tested and those containing La, Pr, Sm and Nd showed a high temperature O_2 desorption peak, aside of a first one at lower temperatures. The authors suggest that the low temperature peak (located between 200 and 600 °C) is due to the reduction of Co^{4+} to Co^{3+}, while the high temperature peak is related to the thermal reduction of Co^{3+} to Co^{2+}. This interpretation also fairly fits the present results, being the weight loss related first to the reduction of Co^{4+} to Co^{3+} and then to that of Co^{3+} to Co^{2+}: this association may be confirmed by the presence of two distinct peaks in the cooling branch of the TPO. The existence of three peaks in the heating

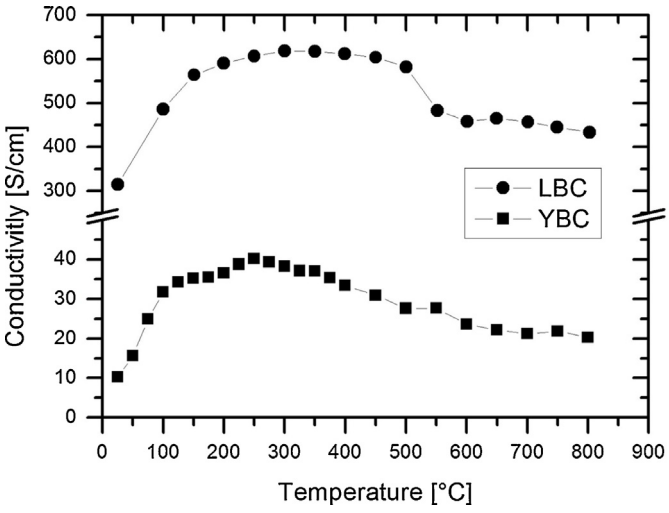

Fig. 8. Electrical conductivity as a function of temperature.

branch is possibly linked to the chemical contour of the Co ions in the crystal structure, that is, a surface Co ion could be more easily accessed and reduced than a Co ion in the bulk, giving rise to additional features in the TPO profile. Alternatively, the two early peaks (at 852 °C and 862 °C) could be related to the reduction of Co ion in the two different crystal structures revealed by the XRD refinement (cubic and tetragonal, Section 3.2.2), followed by the reduction of the Co_3O_4 fraction also present in the material (895 °C). At the highest temperature level, the reduction of the bulk Co could have led to modifications or collapse of the layered structure, which then showed a different re-oxidation pattern upon cooling.

3.2. Electrical and electrochemical characterization

The total electrical conductivity of YBC and LBC was determined in air on sintered bars (Section 2.3). The density of each bar was determined by weighting with a buoyancy balance, using water as the wetting media. In the case of YBC, the resulting density value (5.92 g/cm^3) amounted to 96% of the theoretical value determined from the lattice parameters. In the case of LBC, the measured density (6.58 g/cm^3) corresponded to 94% of the theoretical value estimated from lattice parameters. The results ensured that sufficiently high sintering was achieved for both the samples. The plot of the electrical conductivity measured as a function of temperature is reported in Fig. 8. For YBC, the curve shows that the electrical conductivity increases from 10 S/cm at room temperature to a maximum of 40 S/cm, located approximately at 300 °C, and then decreases to 20 S/cm when heating to 850 °C. This behavior is consistent with a transition from a semiconductor-type to metal-type of conductivity, and was previously reported for analogous YBC samples by other authors:[6,27,28] specifically, the results obtained with the present material are in close agreement with Refs.,[6,28] in terms of temperature thresholds and conductivity values. Higher conductivity values are reported in Refs.[5,27] (250 S/cm at 300 °C), though the transition behavior is respected.

In LBC, the absolute conductivity values are much higher; the total conductivity is about 300 S/cm at room temperature, and increases up to about 600 S/cm at around 300 °C. Then, it shows a sharp drop to 450 S/cm at 550 °C, value that is held until 800 °C. Still, the shape of the conductivity curve as a function of temperature largely resembles that of YBC. Conductivity values are in good agreement with those found by Pang et al.[29] for both disordered and ordered LBC structure, and exceed the values obtained by Zhang[6] in all the measured temperature range. Other authors found much higher values, like in Refs.,[5,26] exceeding 1000 S/cm in the low temperature range.

According to the literature, the change in conductivity slope can be associated to a change in the stoichiometry of the material driven by the release of lattice oxygen at high temperature. A simple mechanism is proposed,[27] which reads in Kröger–Vink notation as:

$$2Co_{Co}^{\bullet} + O_O^x \leftrightarrow 2Co_{Co}^x + V_O^{\bullet\bullet} + \frac{1}{2}O_2 \quad (1)$$

The reduction of the Co ions causes a loss of oxygen and forms vacancies in the lattice. When the sample is heated above 300 °C and starts to lose oxygen (as observed in the TG–DTA and TPO cycles of Figs. 6 and 7), the increase in the number of vacancies is responsible for the reduction of the number of charge carriers and in turn of the reduction of the electrical conductivity.

Moreover, due to Ba losses, some Ba deficiency is expected in the perovskite structure of prepared LBC and YBC. As recently discussed[26,30,31] cationic deficiency on the Ba site generates negative defects in the perovskite lattice ($V_{Ba}^{//}$); those have to be compensated by positive defects, and two possible mechanisms are proposed: (i) generation of an equal number of oxygen vacancies ($V_O^{\bullet\bullet}$) or (ii) oxidation of two B site cobalt ions ($2Co_{Co}^{\bullet}$ or $2h^{\bullet}$). The first mechanism has a detrimental effect on the electrical conductivity (on the other hand, it could enhance oxygen transport), while the second one has the opposite effect, increasing the number of electronic charge carriers. From the above measurements, it can be speculated that vacancy formation is the dominant charge compensation defect for Ba deficiency in YBC and LBC; for LBC we are supported in this hypothesis by the work of Pang et al.[26]

3.2.1. EIS measurements: LBC cathode

EIS experiments at open circuit conditions were performed to investigate the variation of the polarization resistance with temperature and O_2 partial pressure. The microstructure of the cell was analyzed with SEM after the measurement: a section is reported in Fig. 9A, which shows the porous LBC layer (~15 μm thick) in contact with the sintered LSGM electrolyte. The layer porosity was estimated from the values of thickness and weight, and amounted to ~65%.

Fig. 10 reports four typical impedance spectra obtained between 800 and 650 °C when feeding air. Panel A of Fig. 11 shows the results of the tests performed at 750 °C at varying the O_2 molar fraction from 100% to 5%. Panel B reports the variation of the impedance spectra with O_2 partial pressure at 750 °C, when using either N_2 or He as the diluent. In

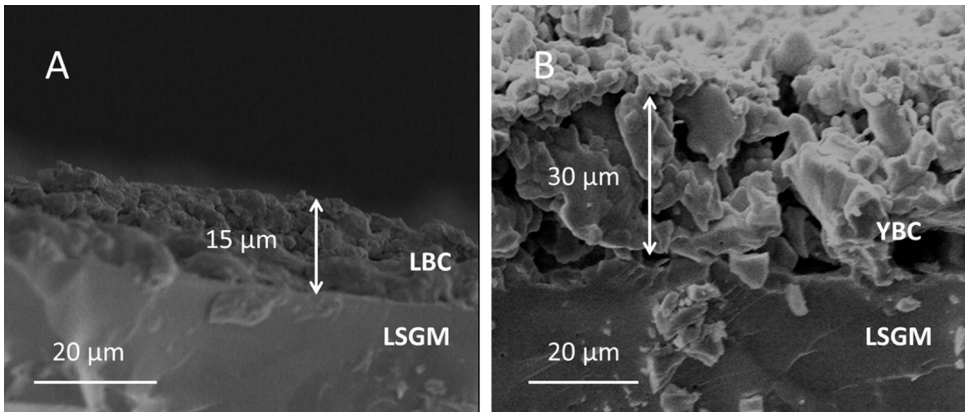

Fig. 9. SEM micrograph showing a part of the cross section of the LBC/LSGM/LBC cell (Panel A, 900× magnification) and of the YBC/LSGM/YBC cell (Panel B, 1000× magnification).

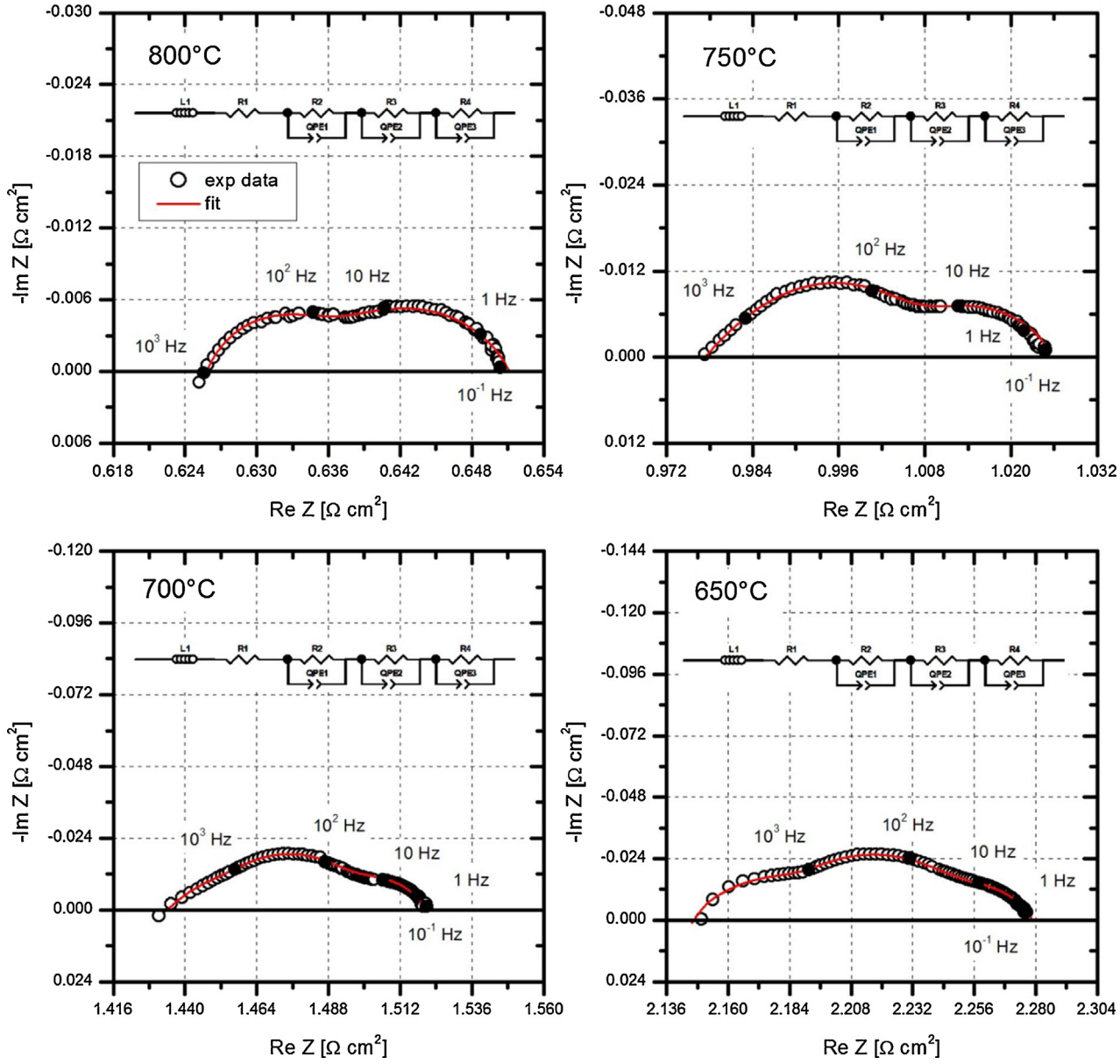

Fig. 10. Complex plane impedance spectra of the LBC/LSGM/LBC symmetrical cell measured between 800 and 650 °C in flowing air (100 Ncc/min). Operating conditions: open circuit conditions, 1 kHz to 0.1 Hz frequency range. Symbols are data, line is fitting.

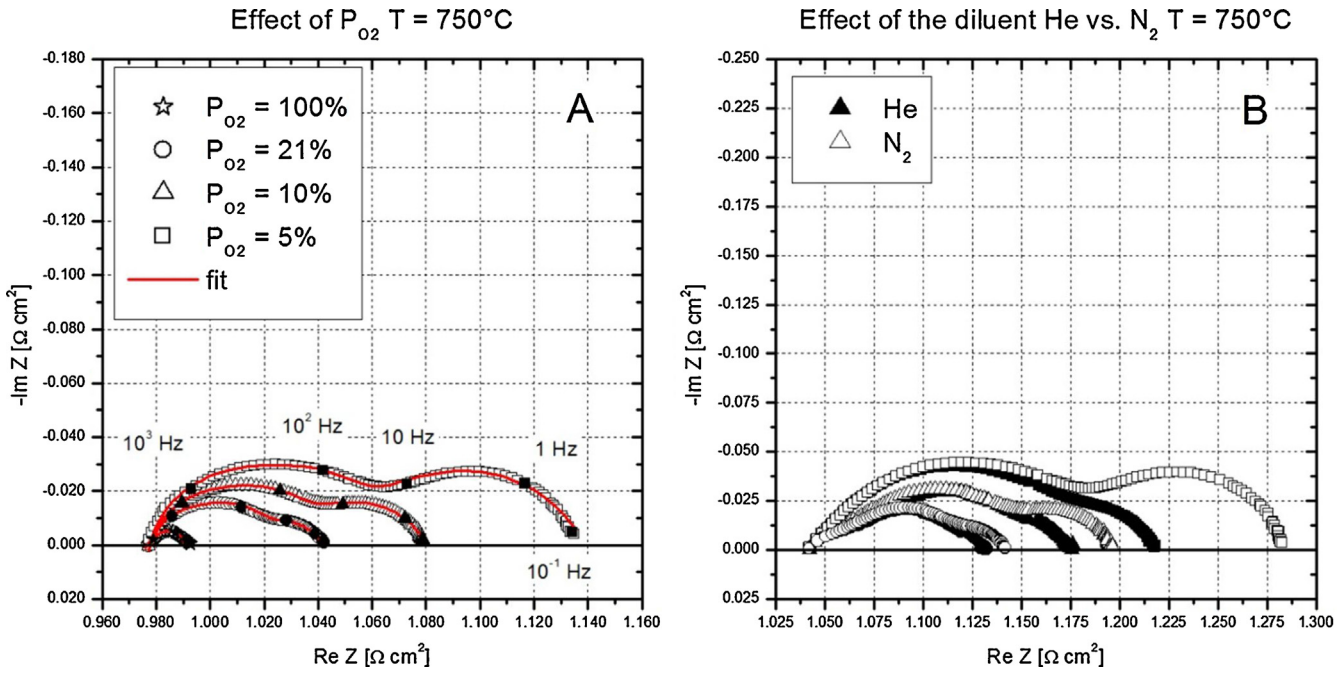

Fig. 11. Complex plane impedance spectra of the LBC/LSGM/LBC symmetrical cell measured at 750 °C. Operating conditions: open circuit conditions, 1 kHz–0.1 Hz frequency range. (Panel A) Effect of O_2 partial pressure. (Panel B) Effect of the diluent, filled symbols are He, open symbols are N_2. (◯ ●) 21% O_2 (v/v); (△ ▲) 10% O_2; (□ ■) 5% O_2.

the figures, all the impedance spectra are normalized by the geometric area of the cathode (0.95 cm^2) and divided by two, coherently with the adoption of a symmetrical cell configuration. At all the temperatures and O_2 fractions, the spectra were fitted with Zview, based on an equivalent circuit of the type $LR_{Ohm}(R_{HF}Q_{HF})(R_{MF}Q_{MF})(R_{LF}Q_{LF})$, reported as an insert in Fig. 10. In the circuit, L is the inductance caused by the electrical equipment and by the leads, R_e is the ohmic resistance mainly due to the electrolyte, while the three remaining RQ elements are associated with processes occurring in the electrodes at high (HF), middle (MF) and low (LF) frequency. The simulated curves are reported as lines in the figures. A very reasonable description was obtained under all the investigated conditions. The values of the fitted parameters are listed in Table 2 for the experiments carried out at varying temperature, and in Table 3 for the experiments performed at 750 °C and varying O_2 partial pressure. For the sake of brevity, only the fitting values and the data collected at 750 °C were reported, which are fully representative of the typical experiment at varying O_2 content. At all the temperatures, the calculations at varying O_2 partial pressure were performed keeping constant the estimate of the ohmic resistance R_{Ohm}. The slight differences between the values at 21% O_2 of Tables 2 and 3 are due to a moderate conditioning effect that involved the cell during the first

Table 2
Fitting parameters for the EIS experiments on the symmetric LBC/LSGM/LBC cell with air flow at varying temperature. Operating conditions as in Fig. 10.

Element	800 °C	750 °C	700 °C	650 °C
L (H)	2.15E−06	2.18E−06	2.48E−06	2.12E−06
R_{ohm} (Ω cm^2)	0.615	0.962	1.396	2.087
R_{HF} (Ω cm^2)	7.18E−03	1.99E−02	4.91E−02	1.06E−01
$QPE_{HF} - Q$ (F cm^{-2})	6.55E−03	2.85E−03	6.68E−04	1.73E−04
$QPE_{HF} - n$	0.956	0.994	0.981	1.003
C_{HF} (F cm^{-2})	4.16E−03	2.70E−03	5.47E−04	1.79E−04
f_{HF} (Hz)	5.33E+03	2.97E+03	5.92E+03	8.36E+03
R_{MF} (Ω cm^2)	1.36E−02	2.44E−02	4.31E−02	9.62E−02
$QPE_{MF} - Q$ (F cm^{-2})	0.0905	0.0565	0.0235	0.0188
$QPE_{MF} - n$	0.801	0.815	0.820	0.819
C_{MF} (F cm^{-2})	1.72E−02	1.27E−02	5.19E−03	4.69E−03
f_{MF} (Hz)	681.06	514.56	711.41	352.89
R_{LF} (Ω cm^2)	1.49E−02	1.96E−02	2.28E−02	3.03E−02
$QPE_{LF} - Q$ (F cm^{-2})	8.083	7.065	2.767	2.673
$QPE_{LF} - n$	0.711	0.711	0.697	0.690
C_{LF} (F cm^{-2})	3.413	3.167	0.888	0.865
f_{LF} (Hz)	3.132	2.562	6.745	6.063

Table 3
Fitting parameters for the EIS experiments on the symmetric LBC/LSGM/LBC cell with air flow at varying O_2 partial pressure at 750 °C. Operating conditions as in Fig. 11.

Element	100%	21%	10%	5%
R_{HF} ($\Omega\,cm^2$)	1.08E−02	1.47E−02	1.87E−02	2.28E−02
$QPE_{HF} - Q$ ($F\,cm^{-2}$)	3.75E−03	7.03E−03	6.66E−03	9.51E−03
$QPE_{HF} - n$	0.994	0.988	0.992	0.994
C_{HF} ($F\,cm^{-2}$)	3.53E−03	6.30E−03	6.20E−03	9.04E−03
f_{HF} (Hz)	4.18E+03	1.72E+03	1.38E+03	7.71E+02
R_{MF} ($\Omega\,cm^2$)	1.53E−02	3.80E−02	5.27E−02	6.48E−02
$QPE_{MF} - Q$ ($F\,cm^{-2}$)	0.1070	0.0398	0.0214	0.0212
$QPE_{MF} - n$	0.820	0.820	0.820	0.820
C_{MF} ($F\,cm^{-2}$)	2.63E−02	6.73E−03	4.85E−03	5.01E−03
f_{MF} (Hz)	395.49	622.57	623.37	490.04
R_{LF} ($\Omega\,cm^2$)	–	2.65E−02	4.84E−02	8.97E−02
$QPE_{LF} - Q$ ($F\,cm^{-2}$)	–	2.803	1.931	1.413
$QPE_{LF} - n$	–	0.705	0.707	0.707
C_{LF} ($F\,cm^{-2}$)	–	0.943	0.724	0.602
f_{LF} (Hz)	–	6.369	4.541	2.947

hours of activity. The values of the relaxation frequency and of the capacitance are also estimated according to the following equations:[32]

$$C_i = \frac{(R_i Q_i)^{1/n}}{R_i} \quad (2)$$

$$f_i = \frac{(R_i Q_i)^{-1/n}}{2\pi} \quad (3)$$

Based on values of Table 2, the Arrhenius plots of the resistances of the HF and MF processes are reported in Fig. 12A. The variation of these resistances with O_2 partial pressure are reported in Fig. 12B and C for all the temperature levels. The reaction order n of the O_2 partial pressure is also reported, estimated according to:

$$R_i \propto P_{O_2}^{-n} \quad (4)$$

With respect to the experiments at varying temperature, the results show that the amplitude of the arcs is always seen to increase as temperature decreases. Concerning the experiments at varying O_2 molar fraction, the polarization resistance increases upon decreasing the O_2 partial pressure, maintaining a double-arc shape: the smallest polarization is observed when feeding pure O_2, which apparently shows only one depressed arc. In the literature, a number of authors have previously investigated the kinetic behavior of LBC cathodes under operating conditions close to the ones adopted in this work. Some authors[25,33] assumed only two RQ elements for the impedance analysis, while other authors assumed either two or three RQ elements depending on the temperature and on the arc shape.[34,35] In our case, three RQ elements were adopted under all tested conditions, coherently with the occurrence of mass transport phenomena in the porous layer, which overlap with the chemical processes. Exclusively in the case of the experiments with pure O_2, two RQ elements were adopted in the equivalent circuit, given that mass transport effects are absent (no N_2 dilution). The occurrence of mass transport resistances was verified under all temperatures by comparing the spectra obtained by using N_2 as the diluent with those obtained by using He: Fig. 11B shows the results of the experiments performed at 750 °C. A variation of the resistance is clearly seen in the arc at low frequency, which reduces upon switching from N_2 (open symbols, smaller O_2 diffusion coefficients) to He (filled symbols, larger O_2 diffusion coefficients) at all the investigated O_2 partial pressures. The same behavior was verified at all the other temperatures, suggesting that the arc at low frequency could be associated with diffusive limitations. The values of the capacitances (0.6–3 $F\,cm^{-2}$) reported in Table 2 and 3 for the LF process are commonly regarded as too high for chemical and electrochemical processes and are generally attributed to gas diffusion processes inside or outside the electrode:[30,35–37] similar results were obtained by Pang et al.[35] on symmetrical cells based on LBC cathodes under conditions close to the present ones and by Pang et al.[30] and Chen et al.[37] on symmetrical cells based on $PrBaCo_2O_{5+\delta}$ cathodes. The correspondence of the LF arc to gas-diffusion in the porous electrode is also supported by the estimated activation energy (0.38 eV) and by the dependence from the O_2 partial pressure, whose order varies between 0.94 at 800 °C and 0.82 at 650 °C. A linear dependence on O_2 partial pressure is indeed expected for gas diffusion,[35] accompanied by a low value of the activation energy, much lower than that typical chemical processes: the present result is fully in line with that reported by Kournoutis et al.[38] (0.35 eV) for LSCF electrodes and within the range of 0.2–0.4 eV reported in the literature by authors working on perovskite based cathodes.

Concerning the other two arcs, the estimated values of the relaxation frequencies (10^4–10^3 Hz) and of the capacitances (10^{-2}–10^{-4} $F\,cm^{-2}$) suggest that the HF arc can be associated to oxygen ion diffusion through the electrode followed by charge transfer at the interface between LBC and LSGM. In line with this association and with the kinetic study of Escudero et al.,[32] the capacitance values increase with temperature (Table 2) and maintain almost constant at increasing the O_2 partial pressure (Table 3). Based on the values of the resistance R_{HF}, the activation energy of the process amounts to 1.51 eV (Fig. 12A), very similar to that of ionic transport in LBC (1.47 eV 25),

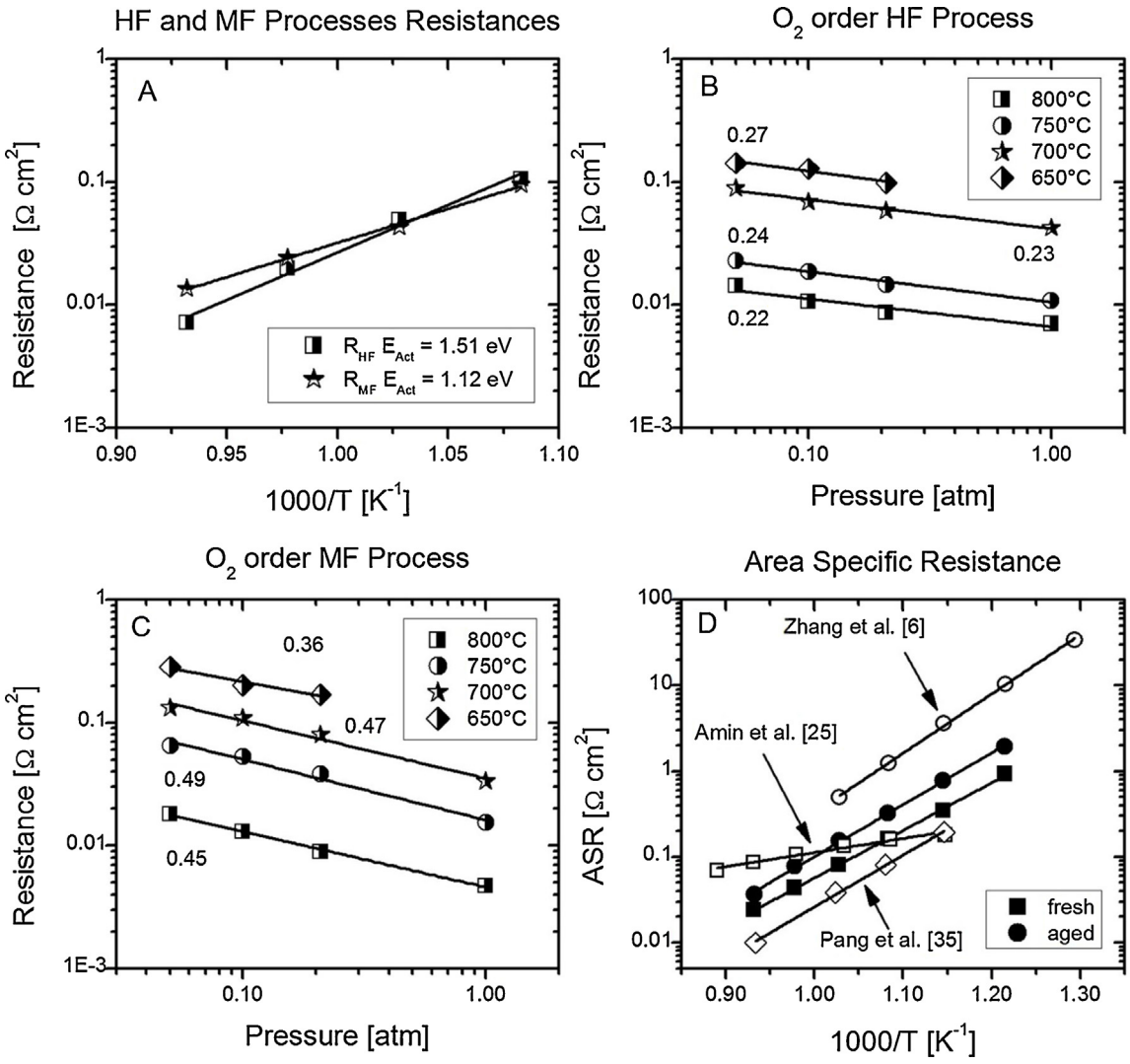

Fig. 12. (Panel A) Arrhenius plot of the resistance of the high frequency (R_{HF}) and middle frequency (R_{MF}) processes of the LBC cathode at $P_{O_2} = 21\%$ (air flow). (Panel B) Dependence of the HF resistance on O_2 partial pressure between 650 and 800 °C. (Panel C) Dependence of the MF resistance on O_2 partial pressure between 650 and 800 °C. (Panel D) Arrhenius plot for the ASR of the LBC cathode on the LSGM electrolyte. Fresh sample (■); aged sample (500 h) (●); Ref.[6] (◯); Ref.[25] (□); Ref.[35] (◊).

while the order of the O_2 partial pressure dependence ranges between 0.27 and 0.22 (Fig. 12B), therefore close to the value of 0.25 typical of processes rate-determined by charge transfer ($O^* + 2e^- + V_o^{\bullet\bullet} \leftrightarrow O^x_o$). The second arc shows values of relaxation frequency between 10^3 and 10^2 Hz (Tables 2 and 3) and values of the capacitance between 10^{-2} and 10^{-3} F cm^{-2}, which increase with temperature (Table 2). In line with the interpretation given in Ref.[32] on perovskite cathodes, the estimated activation energy (1.12 eV, Fig. 12A) and the dependence of O_2 partial pressure (order of 0.49–0.36, Fig. 12C) suggest that a process occurring at the electrode is rate determining, wherein adsorbed atomic oxygen O* is involved possibly via dissociative activation of the adsorbed molecule ($O_2^* \leftrightarrow 2O^*$). Considering these associations, it is worth noting that the resistance values estimated for the HF and MF processes are similar in the whole temperature range (Fig. 12A), with a prevalence of the MF resistance only over 750 °C: this result suggests that the two processes have similar rates and co-limit the reduction mechanism also under steady state conditions.

Relative to the HF process, the present results are in reasonable agreement with those obtained by Pang et al.[35] and by Amin and Karan[25] on symmetric LBC/GDC/LBC cells, as well as those by Setevich et al.[33] for LBC/GDC graded cathodes. In these works, the HF impedance arc is associated to the oxygen ion charge transport at the electrode/electrolyte interface. For this process, Amin and Karan estimated an activation energy of 1.40 eV and found a reaction order of 0.23 at 700 °C, which however decreased to almost zero at 750 and 800 °C, revealing a transition of the rate determining step. A similar behavior was reported by Pang et al.,[35] although with a smaller activation energy (1.35 eV) and a smaller range of the reaction order (0.01–0.103). In a companion paper, dedicated to cation-ordered LBC cathodes,[34] the same authors associated the HF arch to an oxygen ion transport process followed by charge transfer,

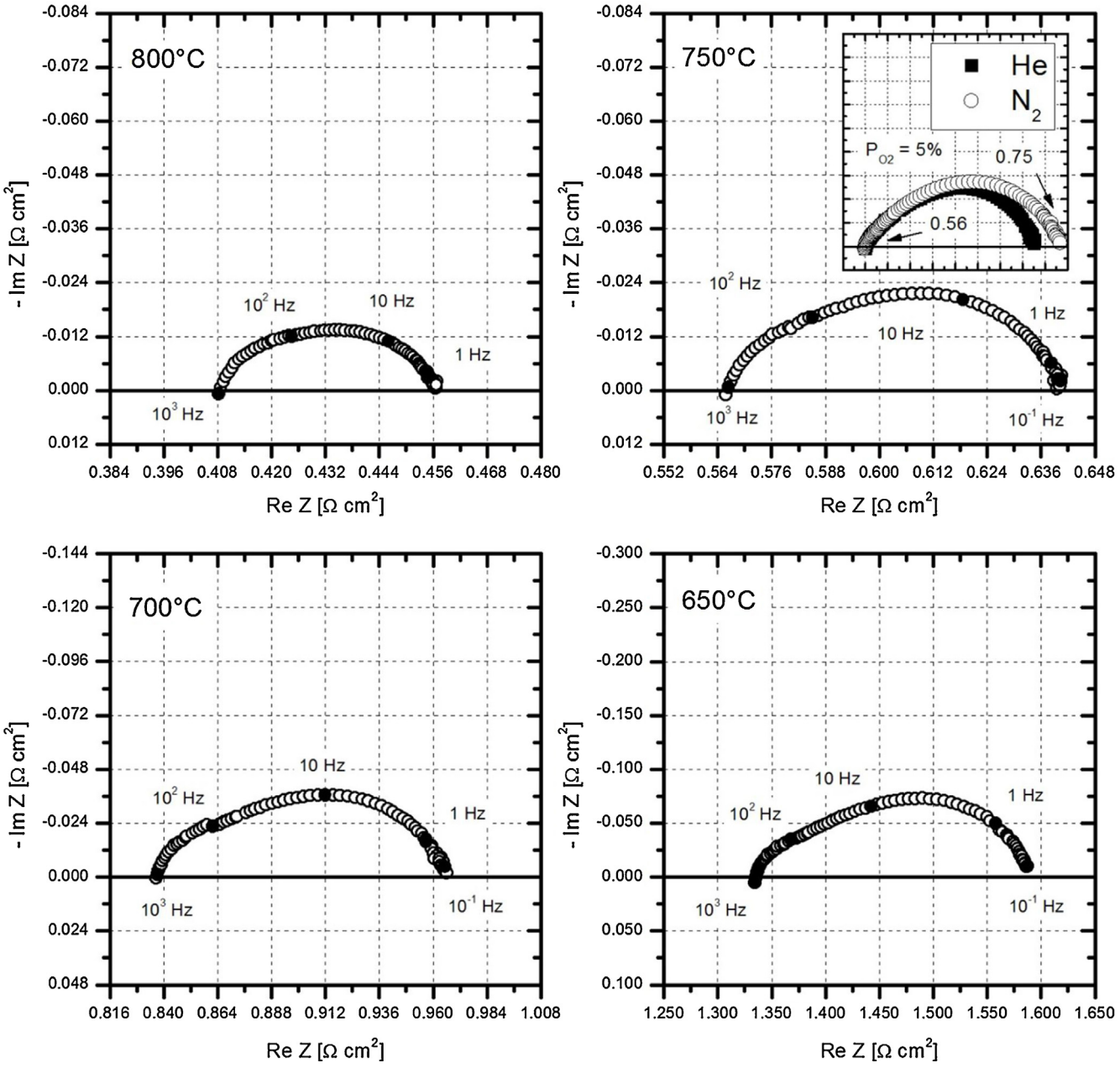

Fig. 13. Complex plane impedance spectra of the YBC/LSGM/YBC symmetrical cell measured between 800 and 650 °C in flowing air (100 Ncc/min). Operating conditions: open circuit conditions, 1 kHz to 0.1 Hz frequency range.

estimating 1.42 eV activation energy, the difference being attributed to the more favorable crystal structure. A wide debate is present in the literature around the MF arc, which is generally associated to processes occurring in the electrode. Pang et al.[35] found an activation energy of 0.87 eV and a reaction order ranging between 0.25 and 0.5 when going from 600 to 700 °C, which was interpreted as an indication that the rate determining step shifted from a charge transfer process (inclusion of O^{2-} in the cathode structure) to a non-charge transfer process (O_2 dissociative activation). Amid and Karan[25] report the occurrence of a surface process, finding an higher order for oxygen (0.77–0.9) and a lower activation energy, almost independent on temperature: this latter result can be possibly due to the equivalent circuit assumed in the analysis (two arcs), which did not allow to separate the contribution of gas-diffusion limitations from the chemical phenomena. Overall, with respect to the mechanistic interpretation of the MF and the HF processes, the differences between the present results and the literature ones (the values of the reaction orders and the absence of a shift) could be a possible indication of a limiting role of the adsorbed oxygen O*. This, on the one hand, could be the result of an enhancement of the oxygen ion vacancies due to the slight Ba deficiency, as reported in Ref.[26] while, on the other hand, it suggests that better performance can

be achieved by increasing the active area for O_2 dissociative adsorption and inclusion in the electrolyte, which is a morphologic characteristic, related mainly to the electrode preparation procedure.

The ASR of the LBC cathode is reported in Fig. 12D, compared against results taken from the literature (empty symbols, □, ◯ and ◊).[6,25,26] For the estimation of the ASR, the polarization resistance was derived from the measured impedance spectra as the difference between the intercepts of the curve with the real axis at low frequency and at high frequency. The squared symbols (■) refer to the fresh cathode, i.e. the cathode at its first exposure to air between 800 and 550 °C. The activation energy amounts to 1.09 eV. This value is in the order of that estimated from the data by Zhang et al.[6] (1.38 eV, LBC/SDC/LBC cells) and close to that found by Pang et al.[26] (1.20 eV on LBC/GDC/LBC cells, no Ba deficiency), while it is much higher than that found by Amin et al.[25] (0.32 eV, LBC/GDC/LBC cells). In line with this, the absolute ASR spans almost two orders of magnitude values. Such a wide range can be due to several factors, namely: the different geometrical and morphologic characteristics of the cathode (thickness, porosity, particle size and microstructure) achieved after the preparation of the cell may have influenced the impact of mass transfer resistances, as well as the characteristics of the interfaces; the use of different electrolytes may have influenced the polarization behavior (for instance, by increasing or decreasing the activation energy of the O^{2-} ion exchange rate); the different crystal structure, in terms of order and disorder properties, may have caused variations in the chemical and electrochemical reaction mechanism and therefore in the global activation energy of the O_2 activation process. Specifically, as reported in Ref.,[34] cation-disordered LBC structures (such as the one obtained in this work and those of Refs. 6,33) are suggested to achieve lower electrochemical performance and higher ASR than cation-ordered ones. It is worthy to note that among the disordered LBC cathodes from the literature (one prepared via combined EDTA-citrate complexing sol–gel process, the other via traditional solid state route), the material prepared in this work shows a lower ASR between 600 and 800 °C, which could suggest that the coprecipitation route may have led to a more favorable chemical structure.

Fig. 12D also reports the ASR of the aged cathode (●), that is, the cathode after 500 h exposure to variable temperature and O_2 partial pressure conditions. The corresponding EIS spectra indicate that the ohmic resistance progressively shifted to higher values and the polarization increased, while maintaining the same number of arcs. An example of this aging process is given in Fig. 11 by comparing the spectra obtained at 750 °C in N_2 at equal O_2 partial pressure on the fresh cathode (panel A, data used for the quantitative analysis) and on the aged cathode (panel B): a shift in the intercept at HF is observed, accompanied by an increase of the value of the intercept at low frequency and a distortion of the first arc. As a consequence of this process, the ASR and the estimated activation energy increased (1.20 eV). The increase in the ohmic and in the polarization resistance could be the result of local disconnections between the porous layer and the sintered electrolyte, due to the large difference in TEC between these two materials, as suggested in Ref.[5] Nonetheless, it is important to note that no delamination was observed and the cell could be fully recovered at the end of the tests. Additionally, the formation of a small amount of the secondary phase formed between LSGM and LBC during the cell firing (as demonstrated by the XRD of Fig. 4B, Section 3.2.2) can have played a role in increasing the ohmic resistance.

3.2.2. *EIS measurements: YBC cathode*

The performance of YBC as a cathode was investigated in air between 450 and 800 °C, at open cell voltage. Experiments were also carried out by using He instead of N_2 as the O_2 diluent. A portion of the cross section of the YBC/LSGM/YBC cell is reported in Fig. 9B, which shows the porous YBC layer in contact with the sintered LSGM electrolyte. The layer porosity was estimated from the values of thickness (∼30 μm) and weight, and amounted to ∼68%.

Fig. 13 reports four of the typical impedance spectra obtained with the cell, only those collected between 800 and 650 °C. One small depressed arc is observed at 800 °C, which becomes progressively bigger upon decreasing the temperature. The shape of the arc is complex and reflects the occurrence of more than one process involved in the reaction of O_2 reduction. Also in this case, a diffusive contribution is present, as demonstrated by the decrease of the polarization resistance upon switching the diluent from N_2 to He, reported in the insert of panel B for the test at 750 °C. Upon decreasing the temperature, a tendency in the growth of the low frequency part of the arc is observed. The low frequency arc becomes thoroughly dominant at lower temperatures possibly indicating a change in the process that limits the reaction rate.

In the case of YBC cathodes, no quantitative equivalent circuit analysis was performed, due to the fact that the activity significantly and quickly decreased with time on stream. Specifically, the ohmic resistance and the polarization resistance were

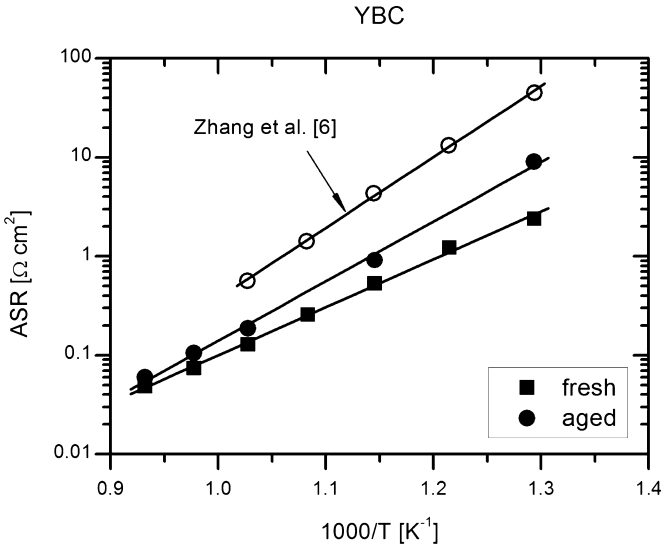

Fig. 14. Arrhenius plot for the ASR of the YBC cathode on the LSGM electrolyte. Fresh sample (■); aged sample (500 h) (●); Ref.[6] (◯).

both seen to grow, while the spectra maintained the same shape and the same number of arcs. The occurrence of degradation phenomena with YBC cathodes has been previously reported in the literature and related to the interaction with the electrolyte, in particular with LSGM,[5] and to the intrinsic instability of the layered perovskite structure.[18] Taken as a whole, however, the spectra obtained on the cathode could be used to estimate the ASR for the fresh (■) and the aged material (● after 500 h in air, Fig. 14). A comparison is also provided with the polarization values reported in the literature for a YBC/SDC/YBC cell tested under conditions analogous to the present ones (◯, from Ref. 6) and prepared by the EDTA-citrate route. On the fresh sample an activation energy of 0.92 eV could be estimated, which grew to 0.98 eV upon aging. In line with the behavior of LBC, however, in the whole temperature range lower polarization resistances are found in the case of the present material, prepared by co-precipitation, with respect to the one from the literature (1.44 eV activation energy).

4. Conclusions

$LaBaCo_2O_{5+\delta}$ and $YBaCo_2O_{5+\delta}$ cathodes were prepared for the first time via simple and facile carbonate co-precipitation synthesis method in aqueous medium. Chemical characterization of both materials showed that the achieved stoichiometry is close to the ideal one, except for a slight Ba deficiency; LBC was obtained as a disordered structure with La and Ba ions randomly distributed on the perovskite A site, while YBC was obtained in the ordered tetragonal phase. TPO and TG–DTA analysis compare well with previous reports about oxygen release and uptake as a function of temperature in these materials. The characterization of the electrical properties of the samples was performed in terms of 4-probe conductivity measurements and EIS tests. Both LBC and YBC electrical conductivities show a transition from low-temperature semiconductor-like to high temperature metal-like behavior, with absolute values in agreement with some previous reports (600 S/cm at 300 °C for LBC, 40 S/cm at 300 °C for YBC), but lower than the highest values obtained in the literature. ASRs of the materials were measured in symmetric cells with LSGM as electrolyte: LBC measured polarization resistance is lower than that reported for similar disordered perovskites. The kinetic analysis of the LBC impedance response revealed that the polarization was mainly contributed at high frequency by oxygen ion diffusion and charge transfer, and at middle frequency by oxygen dissociative adsorption. The slight Ba deficiency in the material could be responsible for both the degradation of the electrical conductivity and the enhancement of the electrochemical activity with respect to similar materials, due to the increased vacancy content. Even though YBC suffered from aging and reactivity with LSGM electrolyte, which led to instability at high temperature, the as-prepared cathode showed increased electrochemical activity with respect to other reports. Overall, the co-precipitation route adopted for the synthesis of LBC and YBC allowed to obtain improved electrochemical activity in symmetric cells and seems promising for the synthesis of IT-SOFC cathode materials, also in light of the eventual improvement or stabilization via doping.

References

1. Maignan A, Martin C, Pelloquin D, Nguyen N, Raveau B. Structural and magnetic studies of ordered oxygen-deficient perovskites $LnBaCo_2O_{5+\delta}$, closely related to the "112" structure. *J Solid State Chem* 1999;**142**:247–60.
2. Zhou W, Lin CT, Liang WY. Synthesis and structural studies of the perovskite-related compound $YBaCo_2O_{5+x}$. *Adv Mater* 1993;**5**:735–8.
3. Chang A, Skinner S, Kilner J. Electrical properties of $GdBaCo_2O_{5+x}$ for ITSOFC applications. *Solid State Ionics* 2006;**177**:2009–11.
4. Tarancón A, Skinner SJ, Chater RJ, Hernández-Ramírez F, Kilner JA. Layered perovskites as promising cathodes for intermediate temperature solid oxide fuel cells. *J Mater Chem* 2007;**17**:3175.
5. Kim JH, Manthiram A. $LnBaCo_2O_{5+\delta}$ oxides as cathodes for intermediate-temperature solid oxide fuel cells. *J Electrochem Soc* 2008;**155**:B385.
6. Zhang K, Ge L, Ran R, Shao Z, Liu S. Synthesis, characterization and evaluation of cation-ordered $LnBaCo_2O_{5+\delta}$ as materials of oxygen permeation membranes and cathodes of SOFCs. *Acta Mater* 2008;**56**:4876–89.
7. Kim JH, Mogni L, Prado F, Caneiro A, Alonso JA, Manthiram A. High temperature crystal chemistry and oxygen permeation properties of the mixed ionic–electronic conductors $LnBaCo_2O_{5+\delta}$ (Ln = Lanthanide). *J Electrochem Soc* 2009;**156**:B1376.
8. Chavez E, Mueller M, Mogni L, Caneiro A. Study of $LnBaCo_2O_{6-\delta}$ (Ln = Pr, Nd, Sm and Gd) double perovskites as new cathode material for IT-SOFC. *J Phys Conf Ser* 2009;**167**:012043.
9. Tarancón A, Burriel M, Santiso J, Skinner SJ, Kilner JA. Advances in layered oxide cathodes for intermediate temperature solid oxide fuel cells. *J Mater Chem* 2010;**20**:3799.
10. Aksenova TV, Gavrilova LY, Tsvetkov DS, Voronin VI, Cherepanov VA. Crystal structure and physicochemical properties of layered perovskite-like phases $LnBaCo_2O_{5+\delta}$. *Russ J Phys Chem A* 2011;**85**:427–32.
11. Taskin AA, Lavrov AN, Ando Y. Achieving fast oxygen diffusion in perovskites by cation ordering. *Appl Phys Lett* 2005;**86**:091910.
12. Manthiram A, Kim J-H, Kim YN, Lee K-T. Crystal chemistry and properties of mixed ionic-electronic conductors. *J Electroceram* 2011;**27**:93–107.
13. Rautama EL, Caignaert V, Boullay P, Kundu AK, Pralong V, Karppinen M, et al. New member of the "112" family, $LaBaCo_2O_{5.5}$: synthesis structure, and magnetism. *Chem Mater* 2008;**21**:102–9.
14. Cristiani C, Zampori L, Latorrata S, Pelosato R, Dotelli G, Ruffo R. Carbonate coprecipitation synthesis of Sr- and Mg-doped $LaGaO_3$. *Mater Lett* 2009;**63**:1892–4.
15. Pelosato R, Cristiani C, Dotelli G, Latorrata S, Ruffo R, Zampori L. Co-precipitation in aqueous medium of $La_{0.8}Sr_{0.2}Ga_{0.8}Mg_{0.2}O_{3-\delta}$ via inorganic precursors. *J Power Sources* 2010;**195**:8116–23.
16. Pelosato R, Cristiani C, Dotelli G, Mariani M, Donazzi A, Natali Sora I. Co-precipitation synthesis of SOFC electrode materials. *Int J Hydrogen Energy* 2013;**38**:480–91.
17. Puigdomenech I. *Hydra/Medusa chemical equilibrium database and plotting software*; 2004.
18. Kim J-H, Kim YN, Bi Z, Manthiram A, Paranthaman MP, Huq A. Overcoming phase instability of $RBaCo_2O_{5+\delta}$ (R = Y and Ho) by Sr substitution for application as cathodes in solid oxide fuel cells. *Solid State Ionics* 2013;**253**:81–7.
19. Rietveld H. A profile refinement method for nuclear and magnetic structures. *J Appl Crystallogr* 1969;**2**:65–71.
20. Larson AC, Dreele RBV. General structure analysis system (GSAS). In: *Los Alamos National Laboratory Report LAUR 86-748.*; 2004.
21. Vogt T, Woodward P, Karen P, Hunter B, Henning P, Moodenbaugh A. Low to high spin-state transition induced by charge ordering in antiferromagnetic $YBaCo_2O_5$. *Phys Rev Lett* 2000;**84**:2969–72.
22. Akahoshi D, Ueda Y. Oxygen nonstoichiometry structures, and physical properties of $YBaCo_2O_{5+x}$ ($0.00 \leq x \leq 0.52$). *J Solid State Chem* 2001;**156**:355–63.

23. Luo W, Wang F. Phase separation in the spin-state transition system of $La_{1-x}Ba_xCoO_3$. *J Solid State Chem* 2009;**182**:3171–6.
24. Fauth F, Suard E, Caignaert V. Intermediate spin state of Co^{3+} and Co^{4+} ions in $La_{0.5}$–$Ba_{0.5}CoO_3$ evidenced by Jahn–Teller distortions. *Phys Rev B: Condens Matter Mater Phys* 2002;**65**:604011–4.
25. Amin R, Karan K. Characterization of $La_{0.5}Ba_{0.5}CoO_{3-\delta}$ as a SOFC cathode material. *J Electrochem Soc* 2010;**157**:B285.
26. Pang SL, Jiang XN, Li XN, Xu HX, Jiang L, Xu QL, et al. Structure and properties of layered-perovskite $LaBa_{1-x}Co_2O_{5+\delta}$ ($x = 0$–0.15) as intermediate-temperature cathode material. *J Power Sources* 2013;**240**:54–9.
27. Xue J, Shen Y, He T. Double-perovskites $YBaCo_{2-x}Fe_xO_{5+\delta}$ cathodes for intermediate-temperature solid oxide fuel cells. *J Power Sources* 2011;**196**:3729–35.
28. McKinlay A, Connor P, Irvine JTS, Zhou W. Structural chemistry and conductivity of a solid solution of $YBa_{1-x}Sr_xCo_2O_{5+\delta}$. *J Phys Chem C* 2007;**111**:19120–5.
29. Pang SL, Jiang XN, Li XN, Wang Q, Zhang QY. Structural stability and high-temperature electrical properties of cation-ordered/disordered perovskite LaBaCoO. *Mater Chem Phys* 2012;**131**:642–6.
30. Pang S, Jiang X, Li X, Wang Q, Su Z. Characterization of Ba-deficient $PrBa_{1-x}Co_2O_{5+\delta}$ as cathode material for intermediate temperature solid oxide fuel cells. *J Power Sources* 2012;**204**:53–9.
31. Pang S, Jiang X, Li X, Wang Q, Su Z, Zhang Q. Highly enhanced electrochemical performance of $PrBa_{0.92}Co_2O_{5+\delta}$ cathode by introducing Ba cationic-deficiency. *Int J Hydrogen Energy* 2012;**37**:3998–4001.
32. Escudero MJ, Aguadero A, Alonso JA, Daza L. A kinetic study of oxygen reduction reaction on La_2NiO_4 cathodes by means of impedance spectroscopy. *J Electroanal Chem* 2007;**611**:107–16.
33. Setevich C, Mogni L, Caneiro A, Prado F. Characterization of the $La_{1-x}Ba_xCoO_{3-\delta}$ ($0 \leq x \leq 1$) system as cathode material for IT-SOFC. *J Electrochem Soc* 2012;**159**:B73.
34. Pang S, Jiang X, Li X, Su Z, Xu H, Xu Q, et al. Characterization of cation-ordered perovskite oxide $LaBaCo_2O_{5+\delta}$ as cathode of intermediate-temperature solid oxide fuel cells. *Int J Hydrogen Energy* 2012;**37**:6836–43.
35. Pang S, Jiang X, Li X, Wang Q, Su Z. A comparative study of electrochemical performance of $La_{0.5}Ba_{0.5}CoO_{3-\delta}$ and $La_{0.5}Ba_{0.5}CoO_{3-\delta}$–$Gd_{0.1}Ce_{0.9}O_{1.95}$ cathodes. *Int J Hydrogen Energy* 2012;**37**:2157–65.
36. Adler SB. Factors governing oxygen reduction in solid oxide fuel cell cathodes. *Chem Rev* 2004;**104**:4791–843.
37. Chen D, Ran R, Zhang K, Wang J, Shao Z. Intermediate-temperature electrochemical performance of a polycrystalline $PrBaCo_2O_{5+\delta}$ cathode on samarium-doped ceria electrolyte. *J Power Sources* 2009;**188**:96–105.
38. Kournoutis VC, Tietz F, Bebelis S. AC impedance characterisation of a $La_{0.8}Sr_{0.2}Co_{0.2}Fe_{0.8}O_{3-\delta}$ electrode. *Fuel Cells* 2009;**9**:852–60.